Geochemical Perspectives Letters

Secular variability in zircon phosphorus concentrations prevents simple petrogenetic classification

C.E. Bucholz[1*], J. Liebmann[2], C.J. Spencer[3]

OPEN ACCESS

https://doi.org/10.7185/geochemlet.2240

Abstract

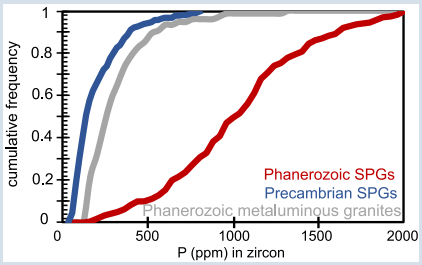

Phosphorus (P) concentrations in zircon have been used to discriminate their derivation from metaluminous *versus* strongly peraluminous granites (SPGs) based on the empirical observation of lower P concentrations in zircon from Phanerozoic metaluminous *versus* peraluminous granites. Higher P concentrations in zircon from Phanerozoic SPGs reflect enhanced apatite solubility in peraluminous melts and overall higher P concentrations in peraluminous granites. However, SPGs derived from partial melting of Precambrian sedimentary rocks have lower P concentrations compared to Phanerozoic metaluminous granites, reflecting lower P concentrations in Precambrian *versus* Phanerozoic sedimentary sources. We demonstrate that zircons from Precambrian SPGs also have lower P concentrations compared to Phanerozoic counterparts, likely reflecting lower P concentrations in their parental melts. Applying the P-in-zircon proxy to the detrital zircon record does not effectively discriminate between metaluminous and peraluminous sources and underestimates contributions from peraluminous granites. Although detrital zircons are an important early Earth archive, a uniformitarian perspective cannot always be applied when using trace element proxies developed on Phanerozoic samples.

Received 5 August 2022 | Accepted 18 October 2022 | Published 11 November 2022

Introduction

Trace element concentrations in zircon are used to "fingerprint" the magma from which they crystallised (*e.g.*, Grimes *et al.*, 2015). Of particular interest is identification of zircon from "I-type" or metaluminous granites *versus* those from "S-type" or strongly peraluminous granites (SPGs[1]; Burnham and Berry, 2017; Trail *et al.*, 2017). Understanding the relative contribution of zircon from metaluminous *versus* peraluminous granites throughout Earth's history yields information on lithologic diversity and tectonic environments through time. SPGs dominantly form in collisional orogenic environments through the partial melting of sedimentary rocks (Nabelek, 2020). Thus, their inferred presence (or absence) through time yields information on both tectonic regimes and the availability of sedimentary rocks to be recycled into magmas during orogenic cycles.

One proposed proxy to discriminate zircon from metaluminous and peraluminous granites is phosphorus (P) concentrations in zircon (Burnham and Berry, 2017). As the solubility of apatite increases with melt aluminium saturation index (Pichavant *et al.*, 1992; Wolf and London, 1994), P concentrates in peraluminous melts during differentiation due to the lack of apatite precipitation (Bea *et al.*, 1994), a trend contrary to that observed in metaluminous melts (Lee and Bachmann, 2014). Indeed, Phanerozoic SPGs have significantly higher P_2O_5 (on average ~0.25 wt. % and up to ~1.5 wt. % P_2O_5; Bea *et al.*, 1992; Bucholz, 2022; Fig. 1a,b) than metaluminous granites (which generally have <0.20 wt. % at bulk rock SiO_2 > 65 wt. %). Further, upon apatite saturation, P concentrations are buffered at higher levels in peraluminous than metaluminous melts.

Consequently, assuming equivalent zircon-melt P partition coefficients for metaluminous and peraluminous granitic systems, zircons from SPGs should have higher P contents than those from metaluminous granitic melts (Burnham and Berry, 2017). Indeed, P in zircons from Phanerozoic peraluminous *versus* metaluminous granites have higher P concentrations (means of 1017 ± 53 *versus* 312 ± 48 ppm (2 s.e.); Burnham and Berry, 2017; Zhu *et al.*, 2020; Fig. 1c,d). Further, P and REE + Y concentrations are strongly correlated in zircon from Palaeozoic SPGs, suggesting the incorporation of P, REE, and Y into the zircon lattice *via* the coupled xenotime-type mechanism $[(Y, REE)^{3+} + P^{5+} = Zr^{4+} + Si^{4+}]$. Based on these observations it has been proposed that P > 750 ppm and (REE + Y) < 1.15*P are robust criteria for identifying zircon from peraluminous granites (Burnham and Berry, 2017).

However, P_2O_5 concentrations in SPGs are not elevated above those of metaluminous granites throughout Earth history

1. Division of Geological and Planetary Sciences, California Institute of Technology, Pasadena, CA 91125
2. School of Earth and Planetary Sciences, Curtin University, 6845, Perth, Australia 6845
3. Department of Geological Sciences and Geological Engineering, Queen's University, Kingston, Canada K7L 3N6
* Corresponding author (email: cbucholz@caltech.edu)

1 We prefer the use of strongly peraluminous granite over "S-type" granites as the former is purely a geochemical definition that avoids confusion associated with the "alphabet" granite classification scheme (*c.f.*, Frost *et al.*, 2001). However, we emphasise that the SPGs discussed here have all been previously demonstrated to have formed *via* the partial melting of metasedimentary rocks.

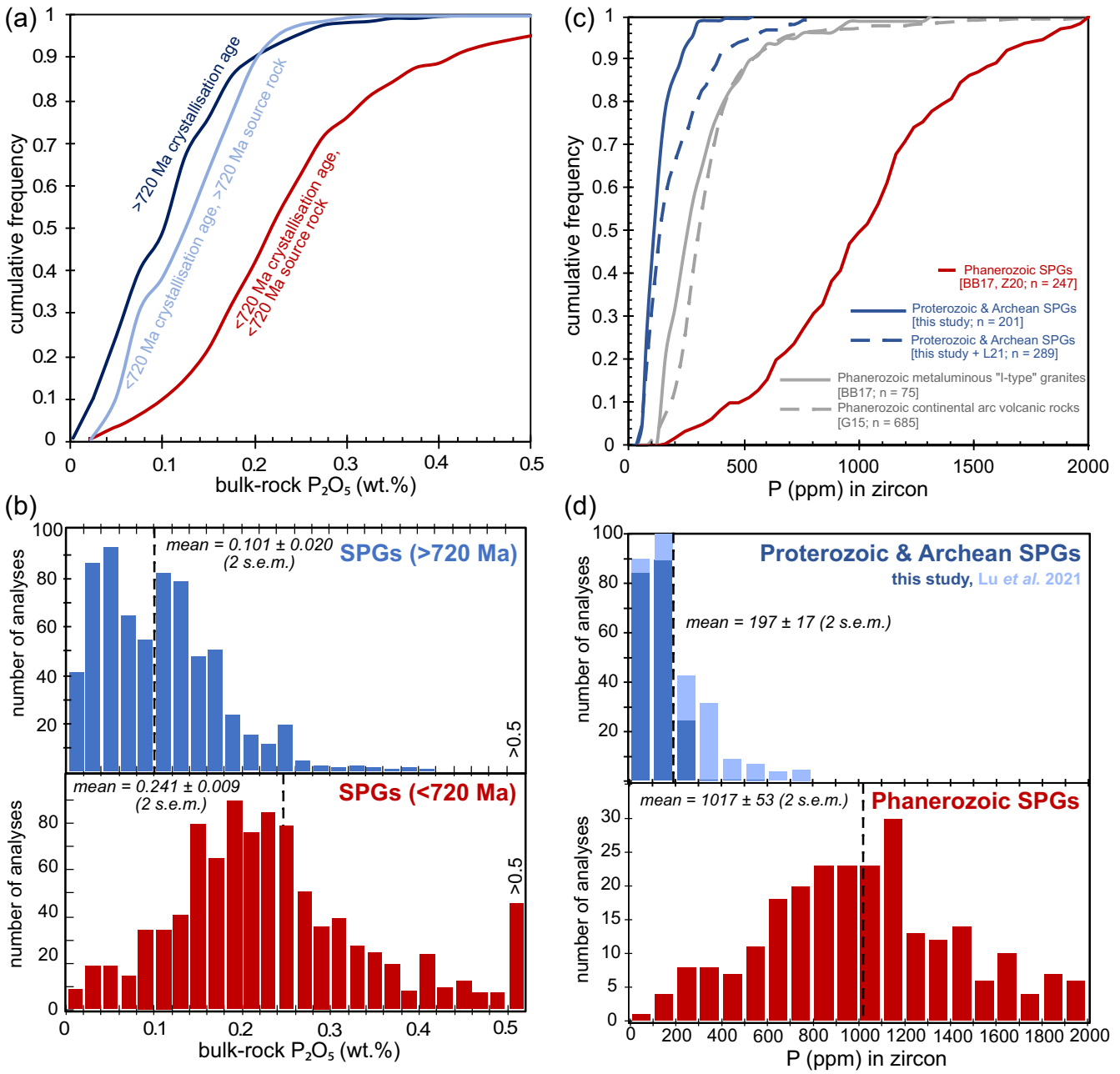

Figure 1 **(a)** Cumulate frequency distributions of SPG bulk rock P_2O_5. **(b)** Histograms of SPG bulk rock P_2O_5 with source rock and crystallisation ages >720 Ma (top) and <720 Ma (bottom). Data in **(a)** and **(b)** from Bucholz (2022). **(c)** Cumulative frequency distributions of P in zircon for Proterozoic and Archean SPGs, as well as Phanerozoic SPGs, "I-type" granites, and continental arc volcanic rocks. **(d)** Histograms of zircon P concentrations for Proterozoic/Archean SPGs and Phanerozoic SPGs. Phanerozoic SPG and I-type granite data in **(c)** and **(d)** are from Burnham and Berry (2017) and Zhu *et al.* (2020) and continental arc volcanic zircon from Grimes *et al.* (2015).

(Bucholz, 2022). Maximum and average P_2O_5 concentrations in SPGs derived from sedimentary rocks deposited after 720 Ma are elevated above those derived from older source rocks (Fig. 1a,b). This temporal variation mirrors a similar increase in P concentrations in marine siliciclastic sediments deposited after 720 Ma, related to increased atmospheric and marine O_2 levels and enhanced authigenic P burial (Reinhard *et al.*, 2017). After considering the factors affecting P concentrations in SPGs, Bucholz (2022) concluded that the temporal change in P concentrations is most likely explained as reflecting higher P concentrations in younger sedimentary source rocks. Elevated P concentrations in SPGs derived from sedimentary rocks deposited after 720 Ma could reflect both higher melt P concentrations and/or inherited P-rich restitic minerals (*e.g.*, apatite, monazite, or P-bearing silicates).

If P concentrations in Archean and most Proterozoic SPGs are relatively low and if this, to some degree, represents lower melt P concentrations, zircon crystallising from such melts may record these low P concentrations. To test this hypothesis, we analysed trace element concentrations (including P) in zircon from Meso- to Paleoproterozoic and Archean SPGs.

Studied Samples and Methods

We analysed trace elements in zircon (n = 201 analyses) from 16 previously characterised SPGs (Liebmann *et al.*, 2021a,b) from

the southwestern USA (*ca.* 1.4 Ga), the North China Craton (*ca.* 1.9 and 2.5 Ga), Finland (*ca.* 1.8–1.9 Ga), and Ghana (*ca.* 2.2 Ga) (see Tables S-1 and S-2 for locality, lithologic, and bulk rock major elements). The average bulk rock P_2O_5 contents of these SPGs are 0.088 ± 0.036 wt. % (2 s.e.). U-Pb isotopes and trace elements (Ca, P, Y, Hf, and REEs) were collected simultaneously using split stream laser ablation inductively coupled plasma mass spectrometry at UC Santa Barbara. Full analytical details are given in the Supplementary Information (SI) and sample and standard analyses are given in Tables S-4 and S-5, respectively. Cathodoluminescence imaging and U-Pb ages were used to ensure analysis of magmatic zircon (*i.e.* related to the crystallisation of the SPG) and not inherited cores/grains (Fig. S-1). Any analyses of inherited cores (with older U-Pb ages) or with >5 % discordance of U-Pb ages were excluded. No apatite inclusions were observed. We are aware of only one other locality of >720 Ma SPGs where trace elements in magmatic zircon were analysed (Lu *et al.*, 2021) and include these data in our discussion.

Results

The P concentrations in Archean and Proterozoic SPGs are positively skewed (average = 132 ± 10 (2 s.e.) ppm; median = 110 ppm; and including Lu *et al.* (2021) data, average = 196 ± 17 ppm; median = 138 ppm). In comparison, P concentrations in zircon from Phanerozoic SPGs are normally distributed with an average of 1017 ± 53 (2 s.e.) (Fig. 1c,d). Cumulative frequency distributions of P concentrations highlight this difference (Fig. 1c) and the mean P concentration in zircon from Precambrian and Phanerozoic SPGs are statistically distinguishable ($P < 0.00001$, Wilcoxon rank sum test). Zircon REE + Y concentrations from Precambrian SPGs, although weakly correlated with P ($R^2 = 0.63$), are defined by a slope of >1.15, distinct from the Phanerozoic SPG trend (Fig. 2). Neither P nor total REE concentrations correlate with Ca concentrations, suggesting that P concentrations are not reflecting the incorporation of apatite inclusions in the ablation volume.

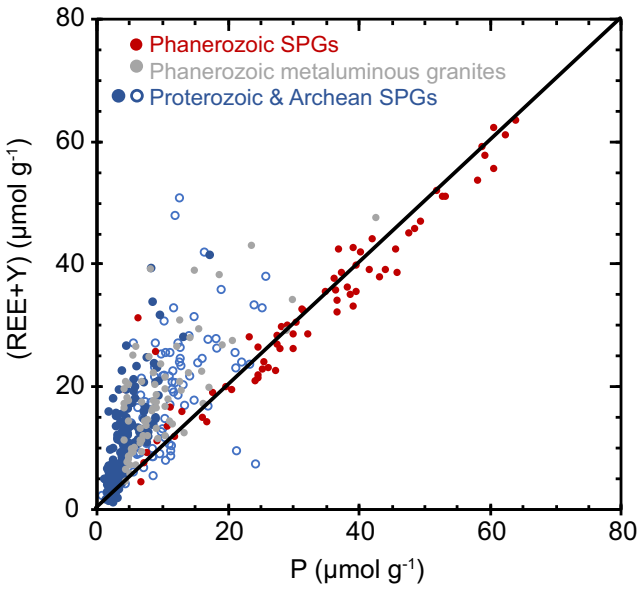

Figure 2 REE + Y *versus* P (in µmol/g) in zircon. Phanerozoic granite data are the same as in Figure 1. Proterozoic and Archean SPGs are from this study (filled symbols) and Lu *et al.* (2021) (open symbols).

What Do Zircon P Concentrations Represent?

The P concentration of zircon reflects equilibrium and/or disequilibrium processes during crystallisation from melt, including (1) equilibrium partitioning dependent on temperature, pressure, and melt composition, (2) partitioning reflecting melt-crystal boundary layer concentrations controlled by diffusion of P in the melt, or (3) surface controlled non-equilibrium growth (*e.g.*, Watson and Liang, 1995; Hofmann *et al.*, 2009). In the first scenario, assuming that P partitioning is both Henrian and that equilibrium between zircon and melt occurred, then lower P concentrations in zircon from Archean/Proterozoic *versus* Phanerozoic SPGs could reflect either lower P concentrations in their parental melts or different conditions of crystallisation (*e.g.*, melt composition, pressure, and temperature) which resulted in variable zircon-melt P partition coefficients. Phosphorus partitioning between melt and zircon as a function of melt composition, temperature, and pressure is poorly understood with limited experimental studies available (Rubatto and Hermann, 2007; Taylor *et al.*, 2015). However, Archean/Proterozoic SPGs are thought to have formed under similar conditions (*e.g.*, pressure, temperature) to those in the Phanerozoic (Bucholz and Spencer, 2019). Thus, in the first scenario of equilibrium partitioning, the simplest explanation is that lower P concentrations in zircon from Archean/Proterozoic SPGs, as compared to Phanerozoic ones, reflect lower melt P concentrations.

In the second scenario, the growth rate of zircon approaches (or exceeds) the diffusivity of P (and/or REE) in the adjacent melt. For hydrous rhyolites (~6 wt. % H_2O), experimentally calibrated P and Zr diffusivities (D) are similar with $\log(D_P)$ and $\log(D_{Zr})$ between −13.5 to −14.5 m^2/s at 750–850 °C (see review of Zhang and Gan, 2022). However, when zircon growth is sufficiently fast, P due to its general incompatibility is excluded from the zircon and builds up in a melt boundary layer. Thus, the growth of new zircon in equilibrium with this boundary layer acquires higher P concentrations elevated above that predicted by equilibrium partitioning with the bulk (*i.e.* far field) melt. However, all else being equal (*e.g.*, P diffusivity and partition coefficients), melts with higher bulk P concentrations would produce boundary layers with higher P concentrations which would be reflected in higher zircon P concentrations.

Finally, in the third scenario, unequivocable evidence for surface controlled, non-equilibrium growth manifests as sector zoning (Watson and Liang, 1995), however (sub-)µm scale oscillatory variations P concentrations have also been attributed to non-equilibrium growth (Hofmann *et al.*, 2009). We generally avoided analysing portions of zircon that exhibited sector zoning (Fig. S-1). However, when analysed, sector zoned zircon had similar P concentrations to other zircon from the sample (*c.f.*, 18IM15b; Fig. S-1). Further, the 25 µm laser spot used homogenised any visible oscillatory zoning (Fig. S-1), providing an integrated P concentration of the ablation volume. In zircon where multiple (2–3) spots were analysed, P concentrations agree within 25 ppm for 70 % and within 50 ppm for 80 % of zircon (Fig. S-3), suggesting that potential local variability induced by non-equilibrium growth was mostly homogenised.

No matter the P incorporation mechanism, our study demonstrates unequivocally that zircons from Archean and Proterozoic SPGs have lower P concentrations on average than their Phanerozoic SPGs (Figs. 1, 2). A parsimonious explanation for this observation is that lower P concentrations in zircons from Precambrian SPGs reflect lower P concentrations of their granitic parental melts. To explore this idea, we modelled melt P_2O_5 and

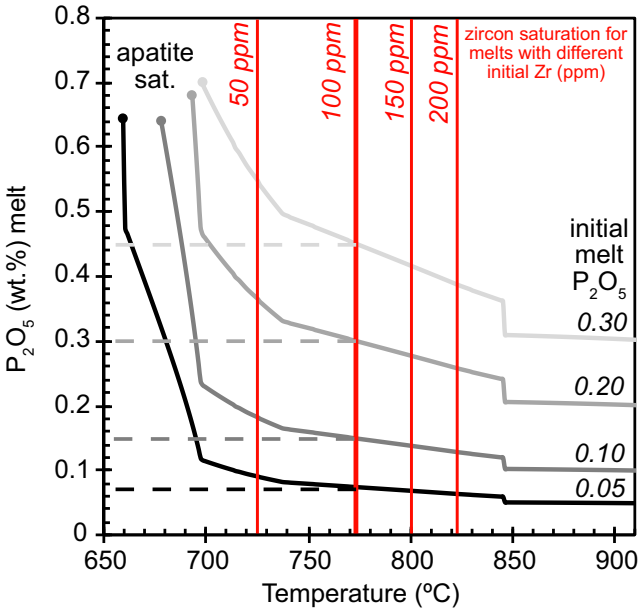

Figure 3 Model results for melt P_2O_5 (wt. %) *versus* temperature during crystallisation of a SPG melt for different initial melt P_2O_5 (wt. %). Melt trajectories end once apatite saturation is reached. Zircon saturation temperatures are indicated with vertical red lines.

zircon and apatite saturation during crystallisation of a SPG melt using alphaMELTS (Pichavant *et al.*, 1992; Smith and Asimow, 2005; Boehnke *et al.*, 2013). Full modelling details are given in the SI. Calculations were performed for initial melt P_2O_5 contents typical of SPGs across Earth history (0.05, 0.10, 0.20, and 0.30 wt. %; Fig. 1a,b).

Due to compositional proximity to the granitic eutectic, zircon saturation temperatures were primarily controlled by increasing Zr concentrations in the melt with progressive differentiation. For initial Zr concentrations in the melt of 50, 100, 150, and 200 ppm, calculated zircon saturation temperatures are ~727, 772, 800, and 822 °C, respectively. [Average Zr concentrations of pre-720 Ma SPGs from Bucholz (2022) are 120 ± 7 ppm (2 s.e.).] The calculated saturation temperatures agree with calculated Ti-in-zircon temperatures which on average are 810 ± 119 °C and 741 ± 105 °C (2 s.d.) assuming a melt TiO_2 activity of 0.5 and 1, respectively (see SI for calculation details). For 100 ppm Zr in the initial melt, modelled melt P_2O_5 concentrations at zircon saturation are 0.08, 0.15, 0.30, and 0.45 wt. % for initial melt P_2O_5 contents of 0.05, 0.10, 0.20, and 0.30 wt. %, respectively (Fig. 3). Importantly, at zircon saturation, the melt P_2O_5 concentration has not significantly increased from its initial value as the melt fraction is still high (~75 %). For a melt with initially low P_2O_5 (0.05–0.10 wt. %) typical for Precambrian SPGs, melt P_2O_5 increases significantly only within 20–30 °C of the granitic eutectic when the melt fraction decreases dramatically. Calculated melts ultimately reach apatite saturation 70–110 °C below that of the zircon saturation for a melt with 100 ppm initial Zr (Fig. 3). Therefore, although melt P_2O_5 increases due to delayed apatite saturation in these peraluminous melts, it remains low at zircon saturation in SPG melts with initially low P contents.

Implications and Conclusion

As SPGs predominantly form during collisional orogenesis, an accurate understanding of their temporal distribution provides information on the tectonic evolution and crustal recycling through time (Bucholz and Spencer, 2019; Frost and Da Prat, 2021). Although detrital zircon can help characterise igneous rocks throughout Earth history, a uniformitarian approach cannot always be applied when using trace element proxies developed on Phanerozoic samples. Specifically, this study provides an example of how temporal variations in sedimentary rocks affect our interpretation of the igneous rock (and mineral) record. For example, the use of zircon P concentrations to identify metaluminous *versus* peraluminous source rocks has been applied to Archean and Hadean detrital zircon (Burnham and Berry, 2017; Zhu *et al.*, 2020). In particular, P and the correlation between P and REE + Y in Jack Hills zircon are more similar to Phanerozoic metaluminous granites and have been used to infer that the Jack Hills zircon crystallised from "TTG-like" magmas (Burnham and Berry, 2017). However, the nature of the source rocks for the Jack Hills zircon is debated with elevated $^{18}O/^{16}O$ ratios (Cavosie *et al.*, 2005; Trail *et al.*, 2007) and Al concentrations in Jack Hills zircon (Ackerson *et al.*, 2021), potentially indicating that some Jack Hills zircons are from granites with a sedimentary source. Our results demonstrate that low P contents and P/(Y + REE) values <1 in Precambrian zircons cannot rule out crystallisation from a peraluminous granitic melt. Therefore, low P contents in Jack Hills zircon is consistent with crystallisation from both metaluminous and peraluminous melts, supporting inferences that the Jack Hills zircon could be sourced from a variety of granitic magmas (Bell, 2017; Ackerson *et al.*, 2021).

Similarly, both cumulative distributions of P contents and P correlations with REE + Y in detrital zircons have been used to infer that SPG formation in the Archean was negligible and limited until the Neoproterozoic to Palaeozoic (Zhu *et al.*, 2020). However, we again urge caution about extrapolating these metrics to Precambrian zircon when sedimentary source regions of SPGs had low P concentrations. Further, Phanerozoic SPGs with sedimentary source rocks deposited before 720 Ma also have low P concentrations (Fig. 1a) and should also contain magmatic zircon with low P. However, P concentrations of detrital zircon may be useful in local studies of young terranes to identify contributions from Phanerozoic P-rich SPGs. Identification of detrital zircon from SPGs with Precambrian source rocks is perhaps best done through a combination of O isotopes with new developing zircon proxies such as Al concentrations (Ackerson *et al.*, 2021) or Si isotopes (Trail *et al.*, 2018).

Acknowledgements

We thank A. Kylander-Clark for his assistance with LA-ICPMS analyses. The constructive reviews of Jesse Reimink and an anonymous reviewer clarified and strengthened our manuscript. This work was supported by NSF grant EAR-1943629 to CB.

Editor: Maud Boyet

Additional Information

Supplementary Information accompanies this letter at https://www.geochemicalperspectivesletters.org/article2240.

Cite this letter as: Bucholz, C.E., Liebmann, J., Spencer, C.J. (2022) Secular variability in zircon phosphorus concentrations prevents simple petrogenetic classification. *Geochem. Persp. Let.* 24, 12–16. https://doi.org/10.7185/geochemlet.2240

References

Ackerson, M.R., Trail, D., Buettner, J. (2021) Emergence of peraluminous crustal magmas and implications for the early Earth. *Geochemical Perspectives Letters* 17, 50–54. https://doi.org/10.7185/geochemlet.2114

Bea, F., Fershtater, G., Corretgé, L.G. (1992) The geochemistry of phosphorus in granite rocks and the effect of aluminium. *Lithos* 29, 43–56. https://doi.org/10.1016/0024-4937(92)90033-U

Bea, F., Pereira, M.D., Corretgé, L.G., Fershtater, G.B. (1994) Differentiation of strongly peraluminous, perphosphorus granites: The Pedrobernardo pluton, central Spain. *Geochimica et Cosmochimica Acta* 58, 2609–2627. https://doi.org/10.1016/0016-7037(94)90132-5

Bell, E. (2017) Ancient magma sources revealed. *Nature Geoscience* 10, 397–398. https://doi.org/10.1038/ngeo2955

Boehnke, P., Watson, E.B., Trail, D., Harrison, T.M., Schmitt, A.K. (2013) Zircon saturation re-revisited. *Chemical Geology* 351, 324–334. https://doi.org/10.1016/j.chemgeo.2013.05.028

Bucholz, C.E. (2022) Coevolution of sedimentary and strongly peraluminous granite phosphorus records. *Earth and Planetary Science Letters* 596, 117795. https://doi.org/10.1016/j.epsl.2022.117795

Bucholz, C.E., Spencer, C.J. (2019) Strongly Peraluminous Granites across the Archean–Proterozoic Transition. *Journal of Petrology* 60, 1299–1348. https://doi.org/10.1093/petrology/egz033

Burnham, A.D., Berry, A.J. (2017) Formation of Hadean granites by melting of igneous crust. *Nature Geoscience* 10, 457–461. https://doi.org/10.1038/ngeo2942

Cavosie, A.J., Valley, J.W., Wilde, S.A., E.I.M.F. (2005) Magmatic $\delta^{18}O$ in 4400–3900 Ma detrital zircons: A record of the alteration and recycling of crust in the Early Archean. *Earth and Planetary Science Letters* 235, 663–681. https://doi.org/10.1016/j.epsl.2005.04.028

Frost, C.D., Da Prat, F.A. (2021) Petrogenetic and tectonic interpretation of strongly peraluminous granitic rocks and their significance in the Archean rock record. *American Mineralogist* 106, 1195–1208. https://doi.org/10.2138/am-2022-8001

Grimes, C.B., Wooden, J.L., Cheadle, M.J., John, B.E. (2015) "Fingerprinting" tectono-magmatic provenance using trace elements in igneous zircon. *Contributions to Mineralogy and Petrology* 170, 46. https://doi.org/10.1007/s00410-015-1199-3

Hofmann, A.E., Valley, J.W., Watson, E.B., Cavosie, A.J., Eiler, J.M. (2009) Sub-micron scale distributions of trace elements in zircon. *Contributions to Mineralogy and Petrology* 158, 317–335. https://doi.org/10.1007/s00410-009-0385-6

Lee, C.-T.A., Bachmann, O. (2014) How important is the role of crystal fractionation in making intermediate magmas? Insights from Zr and P systematics. *Earth and Planetary Science Letters* 393, 266–274. https://doi.org/10.1016/j.epsl.2014.02.044

Liebmann, J., Spencer, C.J., Kirkland, C.L., Bucholz, C., He, X., Santosh, M., Xia, X.P., Martin, L., Evans, N.J. (2021a) Emergence of continents above sea-level influences sediment melt composition. *Terra Nova* 33, 465–474. https://doi.org/10.1111/ter.12531

Liebmann, J., Spencer, C.J., Kirkland, C.L., Bucholz, C.E., Xia, X.-P., Martin, L., Kitchen, N., Shumlyanskyy, L. (2021b) Coupling sulfur and oxygen isotope ratios in sediment melts across the Archean-Proterozoic transition. *Geochimica et Cosmochimica Acta* 307, 242–257. https://doi.org/10.1016/j.gca.2021.05.045

Lu, G.-M., Spencer, C.J., Tian, Y., Wang, W. (2021) Significant Increase of Continental Freeboard During the Early Paleoproterozoic: Insights From Metasediment-Derived Granites. *Geophysical Research Letters* 48, e2021GL096049. https://doi.org/10.1029/2021GL096049

Nabelek, P.I. (2020) Petrogenesis of leucogranites in collisional orogens. *Geological Society, London, Special Publications* 491, 179–207. https://doi.org/10.1144/SP491-2018-181

Pichavant, M., Montel, J.-M., Richard, L.R. (1992) Apatite solubility in peraluminous liquids: Experimental data and an extension of the Harrison-Watson model. *Geochimica et Cosmochimica Acta* 56, 3855–3861. https://doi.org/10.1016/0016-7037(92)90178-L

Reinhard, C.T., Planavsky, N.J., Gill, B.C., Ozaki, K., Robbins, L.J., Lyons, T.W., Fischer, W.W., Wang, C., Cole, D.B. and Konhauser, K.O. (2017) Evolution of the global phosphorus cycle. *Nature* 541, 386–389. https://doi.org/10.1038/nature20772

Rubatto, D., Hermann, J. (2007) Experimental zircon/melt and zircon/garnet trace element partitioning and implications for the geochronology of crustal rocks. *Chemical Geology* 241, 38–61. https://doi.org/10.1016/j.chemgeo.2007.01.027

Smith, P.M., Asimow, P.D. (2005) Adiabat_1ph: A new public front-end to the MELTS, pMELTS, and pHMELTS models: ADIABAT_1PH FRONT-END. *Geochemistry, Geophysics, Geosystems* 6. https://doi.org/10.1029/2004GC000816

Taylor, R.J.M., Harley, S.L., Hinton, R.W., Elphick, S., Clark, C., Kelly, N.M. (2015) Experimental determination of REE partition coefficients between zircon, garnet and melt: a key to understanding high- *T* crustal processes. *Journal of Metamorphic Geology* 33, 231–248. https://doi.org/10.1111/jmg.12118

Trail, D., Mojzsis, S.J., Harrison, T.M., Schmitt, A.K., Watson, E.B., Young, E.D. (2007) Constraints on Hadean zircon protoliths from oxygen isotopes, Ti-thermometry, and rare earth elements. *Geochemistry, Geophysics, Geosystems* 8, Q06014. https://doi.org/10.1029/2006GC001449

Trail, D., Tailby, N., Wang, Y., Mark Harrison, T., Boehnke, P. (2017) Aluminum in zircon as evidence for peraluminous and metaluminous melts from the Hadean to present. *Geochemistry, Geophysics, Geosystems* 18, 1580–1593. https://doi.org/10.1002/2016GC006794

Trail, D., Boehnke, P., Savage, P.S., Liu, M.-C., Miller, M.L., Bindeman, I. (2018) Origin and significance of Si and O isotope heterogeneities in Phanerozoic, Archean, and Hadean zircon. *Proceedings of the National Academy of Sciences* 115, 10287–10292. https://doi.org/10.1073/pnas.1808335115

Watson, E.B., Liang, Y. (1995) A simple model for sector zoning in slowly grown crystals; implications for growth rate and lattice diffusion, with emphasis on accessory minerals in crustal rocks. *American Mineralogist* 80, 1179–1187. https://doi.org/10.2138/am-1995-11-1209

Wolf, M.B., London, D. (1994) Apatite dissolution into peraluminous haplogranitic melts: An experimental study of solubilities and mechanisms. *Geochimica et Cosmochimica Acta* 58, 4127–4145. https://doi.org/10.1016/0016-7037(94)90269-0

Zhang, Y., Gan, T. (2022) Diffusion in Melts and Magmas. *Reviews in Mineralogy and Geochemistry* 87, 283–337. https://doi.org/10.2138/rmg.2022.87.07

Zhu, Z., Campbell, I.H., Allen, C.M., Burnham, A.D. (2020) S-type granites: Their origin and distribution through time as determined from detrital zircons. *Earth and Planetary Science Letters* 536, 116140. https://doi.org/10.1016/j.epsl.2020.116140

Geochemical Perspectives Letters

Secular variability in zircon phosphorus concentrations prevents simple petrogenetic classification

C.E. Bucholz, J. Liebmann, C.J. Spencer

Supplementary Information

The Supplementary Information includes:

- Analytical Methods
- Ti-in-zircon Thermometry
- Zircon and Apatite Saturation Modelling
- Tables S-1 to S-5
- Figures S-1 to S-4
- Supplementary Information References

Analytical Methods

Sample details including name, location, mineralogy, age, and major element composition are given in Tables S-1 and S-2. Cathodoluminescence imaging was previously done by Liebmann *et al*. (2021a, b) and provided in Figure S-1. Analyses were focused on sites with no obvious inclusions or cracks. U-Pb isotopes and trace elements were collected simultaneously on the same zircon volume using split-stream (SS) laser ablation (LA) inductively coupled plasma mass spectrometry (ICPMS) at the University of California, Santa Barabara (Kylander-Clark *et al.*, 2013). Samples were ablated with a Photon Machines 193 nm excimer laser with a HelEx ablation cell coupled to a Nu Instruments Plasma 3D multicollector ICPMS for U-Pb measurements and an Agilent 7700X quadrupole ICPMS for trace element measurements. One analytical session was undertaken in September 2021. A 25 µm spot size was used. The laser fluence at the sample surface was ~1.5 J/cm^2. Each analysis consisted of the laser firing twice followed by a 20 s wash out to remove surface contamination. Zircon were then continuously ablated for 60 shots at a 5 Hz repetition rate, yielding a total ablation time of 12 s.

Every 10 unknown analyses were bracketed by standard zircon 91500 (1062.4 ± 0.4 ID-TIMS $^{206}Pb/^{238}U$ date; Wiedenbeck *et al.*, 1995), which was used as the primary standard for U–Pb isotopic analyses. NIST612 standard reference glass was measured every 30 analyses and used as a primary standard for trace element analyses. Secondary zircon reference materials analysed throughout the session included GJ-1 (601.7 ± 1.3 ID-TIMS $^{206}Pb/^{238}U$ date; Jackson *et al.*, 2004; Kylander-Clark *et al.*, 2013), Plešovice (337.13 ± 0.37 ID-TIMS $^{206}Pb/^{238}U$ date; Sláma *et al.*, 2008), OG-1 (3467.1 ± 0.6 Ma $^{206}Pb/^{238}U$ date; Stern *et al.*, 2009), FC1 (1099.3 ± 0.7 Ma $^{206}Pb/^{238}U$ date; Paces and Miller, 1993), and R33 (419.26 ± 0.39 Ma $^{206}Pb/^{238}U$ date; Black *et al.*, 2004). BHVO standard glasses were also analysed at the beginning, end, and throughout the analytical session. We obtained $^{207}Pb/^{206}Pb$-corrected $^{206}Pb/^{238}U$ concordia dates of 599.5 ± 28.0 Ma (2 s.d., n = 13) for GJ-1, 331.6 ± 9.8 Ma (2 s.d., n = 7) for Plešovice, 3462.7 ± 52.9 Ma (2s.d., n = 7) for OG, 1081.4 ± 31.1 Ma (2 s.d., n = 6) for FC1, and 418.6 ± 19.4 Ma (2 s.d., n = 7) for R33, which are accurate to -0.36 %, -1.64 %, -0.13 %, -1.62 %, and -0.16 % of their reference values, respectively. Standard analyses are given in Table S-5.

For trace-element analyses, ^{90}Zr (assuming ~43.14 wt. % Zr) was used as an internal standard and peaks were measured at ^{27}Al, ^{44}Ca, ^{28}Si, ^{31}P, ^{49}Ti, ^{89}Y, ^{90}Zr, ^{93}Nb, ^{139}La, ^{140}Ce, ^{141}Pr, ^{146}Nd, ^{147}Sm, ^{153}Eu, ^{157}Gd, ^{159}Tb, ^{163}Dy, ^{165}Ho, ^{166}Er, ^{169}Tm, ^{172}Yb, ^{175}Lu, and ^{178}Hf. The zircon standards with the most completely characterised trace element concentrations are 91500 (Wiedenbeck *et al.*, 2004) and GJ-1 (Piazolo *et al.*, 2017). Reference P concentrations in these standards are 24 ± 1 ppm (Jochum *et al.*, 2005) and 30.2 ± 12.8 (Piazolo *et al.*, 2017), which compare favourably with our average of 31.5 ± 4.5 ppm and 35.4 ± 4.5 ppm (2 s.d.). For 91500, measured Y and REE concentrations are within ~10 % of reference values (Wiedenbeck *et al.*, 2004) except for Pr (-52 %), Nd (-17 %), and Lu (-15 %) (Table S-3; Figure S-2).

Data reduction follows that of Garber *et al.*, (2020). Briefly, Iolite plug-in version 2.21 (Paton *et al.*, 2011) for the Wavemetrics Igor Pro software was used to correct measured isotopic ratios and elemental intensities for baselines, laser- and plasma-induced fractionation, and drift. Both errors associated with laser stability throughout each analysis and run, as well as detector counting statistics were considered in the reported uncertainties. Only zircon analyses with >95 % concordance were included in the final data set. U-Th-Pb and trace element data are given in Table S-4.

Ti-in-zircon Thermometry

Temperatures for each zircon analysis were calculated via Ti-in-zircon thermometry (Ferry and Watson, 2007):

$$\log (\text{ppm Ti}) = 5.711 \pm 0.072 - 4800(\pm 86)/T\,(\text{K}) - \log(a_{SiO2}) + \log(a_{TiO2})$$

a_{SiO2} was assumed to be 1 (although it may be below unity during early zircon crystallisation when a granitic melt is not quartz saturated near their liquidus). The Ti-in-zircon expression was evaluated for both a_{TiO2} values of 1 and 0.5. A recent thermodynamic study by Schiller and Finger (2019) demonstrated that a_{TiO2} in strongly peraluminous granitic melts is often well below unity near 0.5. Calculated temperatures are given in Table S-4.

Zircon and Apatite Saturation Modelling

We modelled the equilibrium crystallisation of sample CO-17-8, a representative Proterozoic strongly peraluminous granite using alphaMELTS (Smith and Asimow, 2005). The sample modelled composition in wt. % was 71.74 SiO_2, 0.39 TiO_2, 14.61 Al_2O_3, 2.70 FeO(total), 0.50 MgO, 1.26 CaO, 2.60 Na_2O, 5.88 K_2O, 3.00 H_2O. Crystallisation modelling was conducted a 0.3 GPa from 930 to 650 ºC at an oxygen fugacity one log unit below the fayalite-magnetite-quartz buffer. P_2O_5 and Zr were not modelled using alphaMELTS, but rather assumed to behave incompatibly until apatite saturation was reached. Although other major silicate phases such as plagioclase and alkali feldspar can be important reservoirs for P in some strongly peraluminous granites (London, 1992), P incorporation is not considered in these phases for simplicity. We modelled 4 different starting P_2O_5 contents of 0.05, 0.1, 0.2, and 0.3 wt. % and assumed a starting concentration of 100 ppm for Zr, in the range of that typical for SPGs (Bucholz and Spencer, 2019). We used the apatite saturation model of Pichavant *et al.* (1992) and the zircon saturation model of Boehnke *et al.* (2013). Although other phosphates (*e.g.*, monazite and xenotime) will influence the P budget of a crystallising peraluminous melt, we do not consider it in our models because its effect (as compared to apatite) is expected to be negligible. Monazite is indeed found in many strongly peraluminous granites and, like xenotime, its solubility is much lower than apatite (generally saturating at several hundredths of a wt. % P_2O_5). However, its solubility is also strongly controlled by the availability of REE (Stepanov *et al.*, 2012) which limits the amount of monazite that can crystallise to trace amounts. Due in part to this fact and that it has a lower P_2O_5 concentration (~29 wt. %) as compared to apatite (~42 wt. %) it does not contribute significantly influence the P budget of a crystallising melt (*e.g.*, Wolf and London, 1995). Alkali feldspars can also incorporate several tenths up to ~1 wt. % P_2O_5 (London, 1992) however the partitioning of P between granitic melts and alkali feldspar is not well enough understood to model quantitatively. alphaMELTS has been shown to model biotite Fe/Mg ratios and saturation temperatures well in strongly peraluminous granites (Bucholz *et al.*, 2018), however it has more difficulty predicting saturation of other aluminous phases typically found in strongly peraluminous granites

(*e.g.*, muscovite and garnet). However, for the purposes of zircon saturation, the “M" factor [or normalised molar (Na+K+2Ca)/(Al*Si)] used in calculating saturation temperatures (c.f. Boehnke *et al.*, 2013) does not vary significantly (between 1.25 to 0.94 over the temperature interval of interest (broadly 700-900 ºC) (see Fig. S-4) and is primarily a function of increasing ASI during melt differentiation. ASI is expected to increase during differentiation of strongly peraluminous granites (*e.g.*, Bea *et al.*, 1994) and alphaMELTS predicts this well. Similarly, ASI is the primary control on apatite solubility (other than temperature) and our modelling results should reproduce apatite saturation behaviour well.

The vertically zoned Pedrobernardo pluton (central Spain) is a natural example of closed system, *in-situ* differentiation of a strongly peraluminous granitic melt (Bea *et al.*, 1994) and is a useful comparator dataset for our alphaMELTS modelling. Magmatic differentiation in the Pedrobernardo pluton results in increases in bulk-rock SiO_2 from ~71 to 76 wt. % and P_2O_5 from 0.28 to 0.5-0.6 wt. % from biotite+muscovite granites in the lower zone of the pluton to muscovite-bearing aplites and pegmatites of the upper zone. Bulk-rock ASI increases from ~1.18-1.20 to 1.30 and M decreases from 1.16-1.36 to 0.88-0.99. Although the alphaMELTS calculations were undertaken for a different bulk-rock composition and we also recognise that bulk-rock granite chemistry is likely not representative of melt compositions, the broad variations in geochemistry for the Pedrobernardo pluton are similar the calculated melt compositions using alphaMELTS (see Fig. S-4). Thus, we suggest that alphaMELTS models apatite and zircon saturation satisfactorily for the purposes of this study, though a more detailed future study is warranted. Last, we do recognise that the temperatures of apatite and zircon saturation may not be accurate if the alphaMELTS is not predicting the correct temperatures of crystallisation for different mineral assemblages. However, the important point is that zircon saturation will precede that of apatite and for granitic melts with low initial P_2O_5 concentrations and P_2O_5 concentrations will still be low at the onset of zircon saturation.

Supplementary Tables

Table S-1 List of strongly peraluminous granite samples form which zircon was separated and analysed with locality, mineralogy, and magmatic crystallisation ages. References are given for geochronology of samples, bulk-rock geochemistry, and detailed petrologic descriptions.

Sample ID	Locality	Mineralogy	Age ± 2σ (Ma)	Reference
17FIN04A	Turku Area, Finland	Grt+Bt+Afs+Pl+Bt	1850	Liebmann *et al.*, 2021b
17FIN06A	Turku Area, Finland	Grt+Bt+Afs+Pl+Bt	1815±16	Liebmann *et al.*, 2021b
17FIN06B	Turku Area, Finland	Grt+Bt+Afs+Pl+Bt	1815±16	Liebmann *et al.*, 2021b
18IM-3	Huaian Complex, North China Craton	Grt+Ms+Qz+Afs+Pl±Bt	1917±70	Liebmann *et al.*, 2021a
18IM-12B	Jining Complex, North China Craton	Grt+Qz+Afs+Pl	1929±29	Liebmann *et al.*, 2021a
18IM-13C	Xiwulanbulang Area, North China Craton	Grt+Bt+Qz+Afs+Pl±Ms	2536±13	Liebmann *et al.*, 2021a
18IM-15B	Xiwulanbulang Area, North China Craton	Grt+Qz+Afs+Pl	2530±60	Liebmann *et al.*, 2021a
18IM-19A	Daqingshan-Wulashan Complex, North China Craton	Grt+Bt+Qz+Afs+Pl	2478±18	Liebmann *et al.*, 2021a
18IM-19C	Daqingshan-Wulashan Complex, North China Craton	Grt+Bt+Qz+Afs+Pl	2478±18	Liebmann *et al.*, 2021a
18IM-20	Daqingshan-Wulashan Complex, North China Craton	Grt+Bt+Qz+Afs+Pl	2374±48	Liebmann *et al.*, 2021a
18IM-21C	Daqingshan-Wulashan Complex, North China Craton	Grt+Qz+Afs+Pl	1855±16	Liebmann *et al.*, 2021a
18IM-23D	Daqingshan-Wulashan Complex, North China Craton	Grt+Qz+Afs+Pl	2453±11	Liebmann *et al.*, 2021a
18IM-25C	Daqingshan-Wulashan Complex, North China Craton	Ms+Qz+Afs+Pl±Bt	2493±28	Liebmann *et al.*, 2021a
CO-17-8	Silver Plume granite, Colorado, USA	Ms+Bt+Qz+Afs+Pl	1447±50	(Bucholz and Spencer, 2019; Liebmann *et al.*, 2021b)
19GH-9	Baoulé-Mossi domain, West African Craton	Ms+Bt+Qz+Afs+Pl	2183±12	Liebmann *et al.*, 2021c
19GH-11B	Baoulé-Mossi domain, West African Craton	Ms+Bt+Qz+Afs+Pl	2188±20	Liebmann *et al.*, 2021c

Mineral abbreviations: Qz, quartz; Afs, alkali feldspar; Pl, plagioclase; Grt, garnet; Ms, muscovite, Bt, biotite

Table S-2 Sample bulk-rock major element geochemistry (normalised to 100 %) (originally reported in Liebmann *et al.*, 2021a, b).

Sample	SiO_2	TiO_2	Al_2O_3	FeO^T	MnO	MgO	CaO	Na_2O	K_2O	P_2O_5	Total
18IM3	78.77	0.38	11.05	2.75	0.05	0.88	1.05	2.26	2.76	0.05	100
18IM21C	83.28	0.04	8.91	2.60	0.18	0.66	1.13	2.23	0.78	0.19	100
17FIN06B	71.40	0.06	15.16	3.53	0.04	0.73	1.49	3.17	4.32	0.10	100
17FIN04A	71.61	0.23	14.70	3.23	0.07	0.96	1.63	3.05	4.44	0.08	100
17FIN06A	66.14	0.67	16.31	6.35	0.05	2.25	1.65	2.98	3.52	0.07	100
19GH11B	74.12	0.08	14.81	0.50	0.01	0.15	1.26	3.41	5.66	0.01	100
19GH9	73.70	0.11	15.77	0.96	0.02	0.28	2.93	5.05	1.15	0.03	100
CO-17-8	71.74	0.39	14.61	2.70	0.03	0.50	1.26	2.60	5.88	0.28	100
18IM-13C	72.39	0.34	15.19	2.82	0.01	0.89	3.11	3.37	1.77	0.10	100
18IM-19	73.14	0.32	14.25	3.20	0.05	1.43	1.29	2.52	3.73	0.06	100
18IM-15B	67.10	0.60	15.92	6.49	0.09	2.18	3.62	2.92	0.99	0.09	100
18IM-25C	75.81	0.06	13.41	0.87	0.00	0.17	0.97	2.76	5.91	0.03	100
18IM-23D	72.83	0.11	14.26	2.58	0.04	0.80	0.61	2.04	6.61	0.12	100
18IM20	64.68	0.27	18.10	5.61	0.07	1.84	2.68	3.57	3.11	0.07	100
18IM12B	70.78	0.14	15.10	5.50	0.13	1.95	2.92	2.38	1.06	0.04	100

Table S-3 Phosphorus values of zircon standards compared to reference values.

zircon standard	P (ppm) reference value	2 s.d.	P (ppm) measured	2 s.d.*	# of analyses
91500	24[3]	1	31.5	4.5	42
GJ-1	30.2[4]	12.8	35.4	4.4	13

*propagated error including internal precision and standard deviation of analyses

Table S-4 Zircon LA-ICPMS U-Th-Pb isotopes and trace element data. Table S-4 (.xlsx) can be downloaded from the online version of this article at https://doi.org/10.7185/geochemlet.2240

Table S-5 Standard LA-ICPMS U-Th-Pb isotopes and trace element data. Table S-5 (.xlsx) can be downloaded from the online version of this article at https://doi.org/10.7185/geochemlet.2240

Supplementary Figures

Figure S-1 Cathodoluminescence images of analysed zircon with sample number in the heading and grain number labelled on each image, showing LA-ICPMS spots (red circles) and P concentrations (ppm) listed.

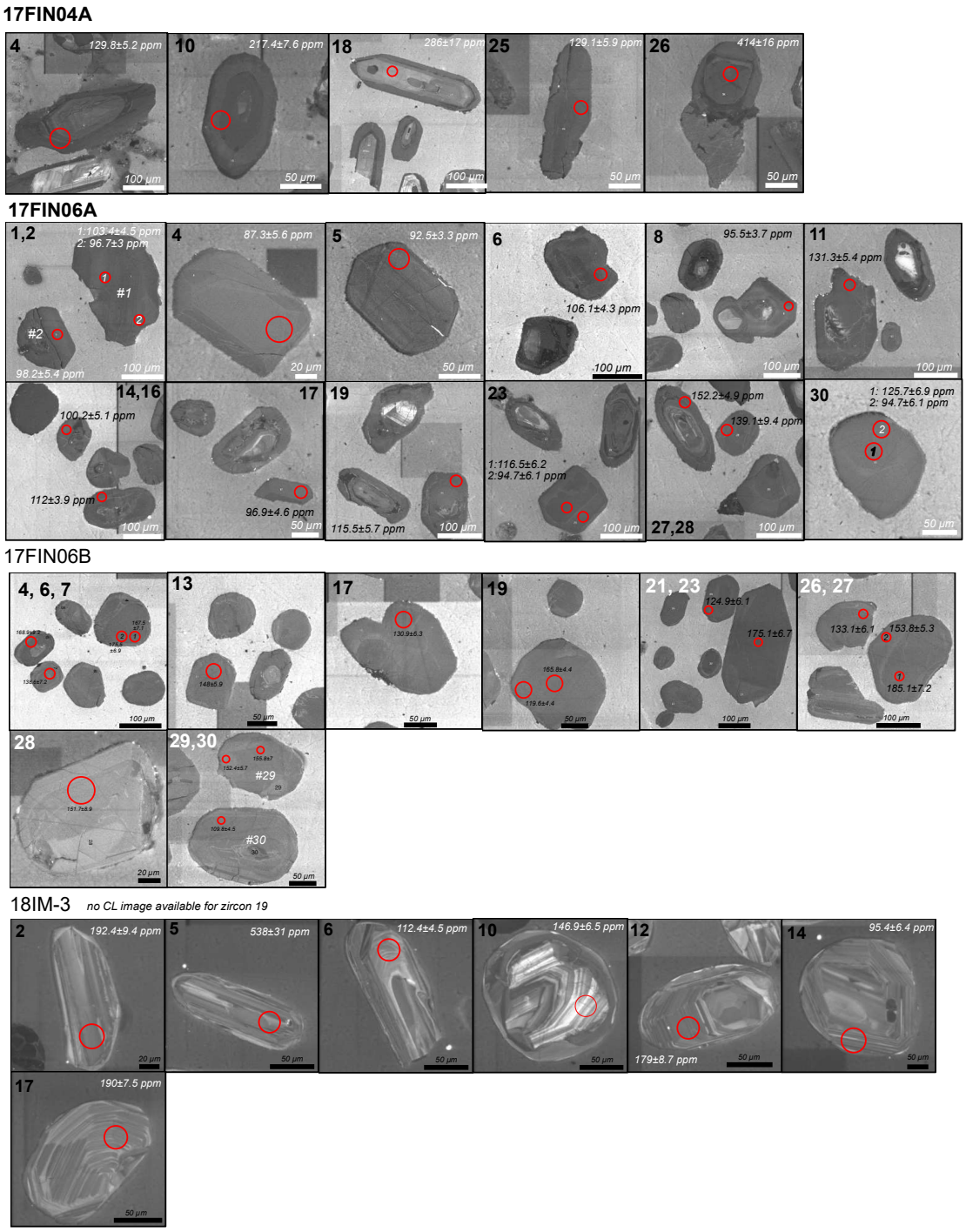

18IM15b

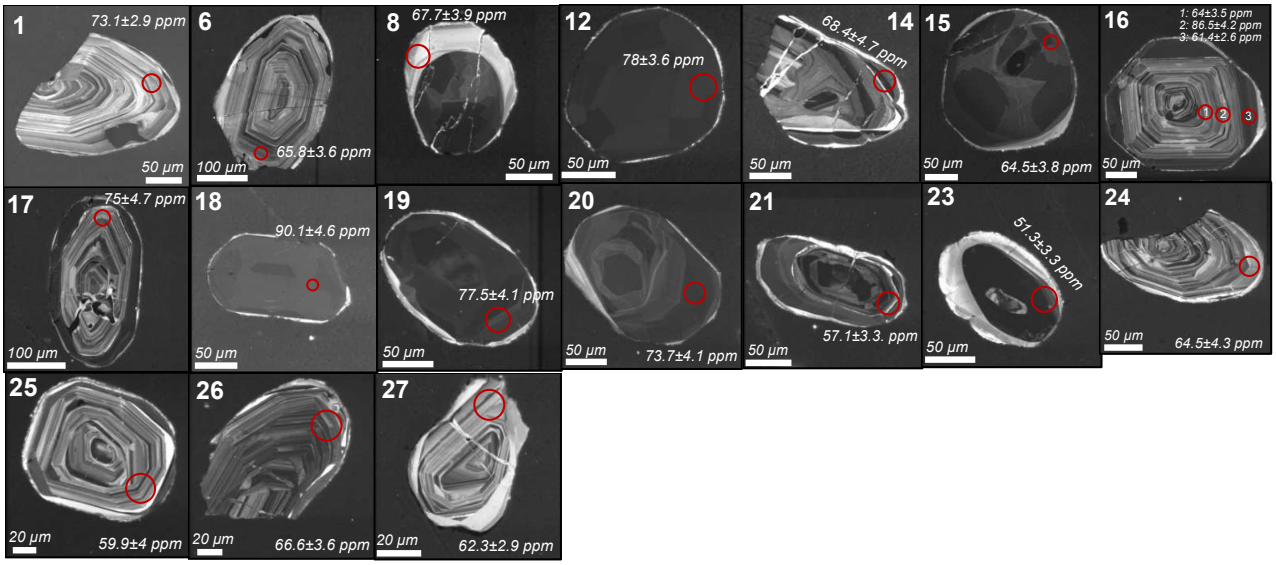

18IM13c

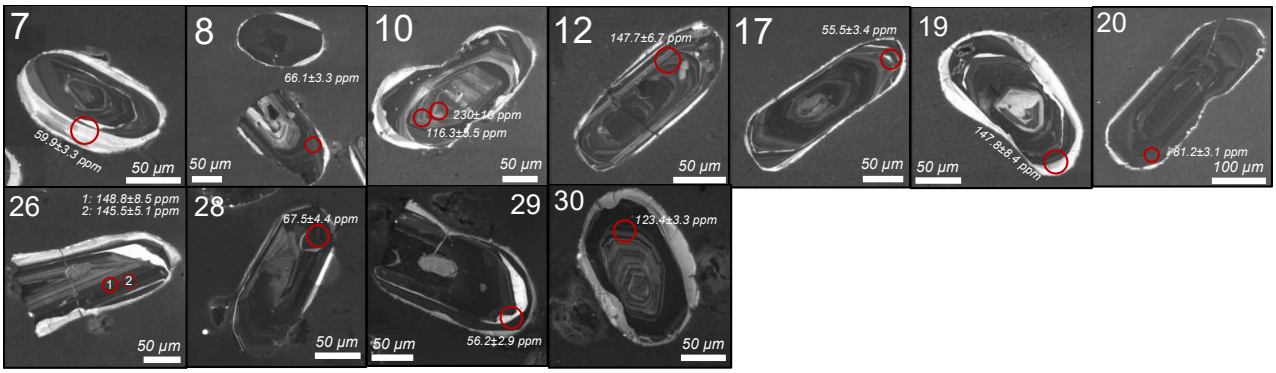

18IM25c

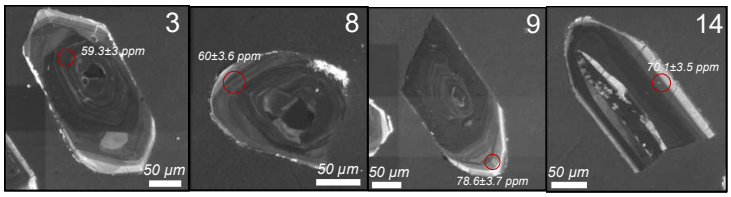

18IM12b

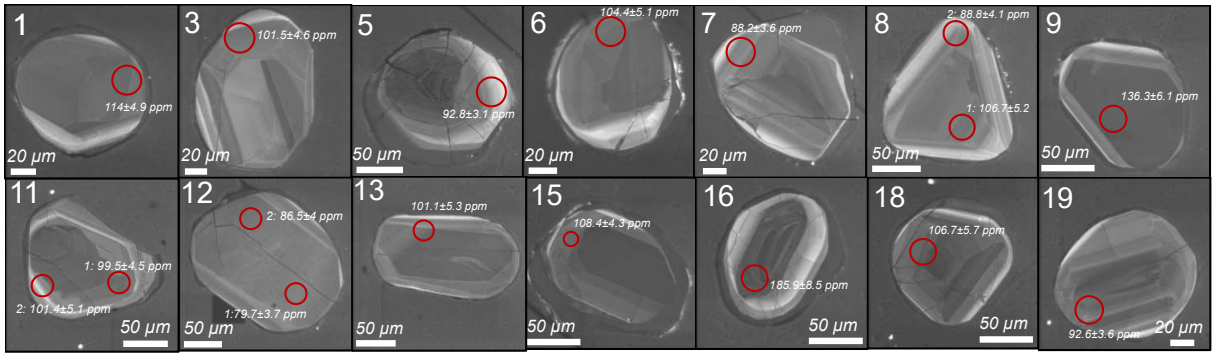

18IM19a

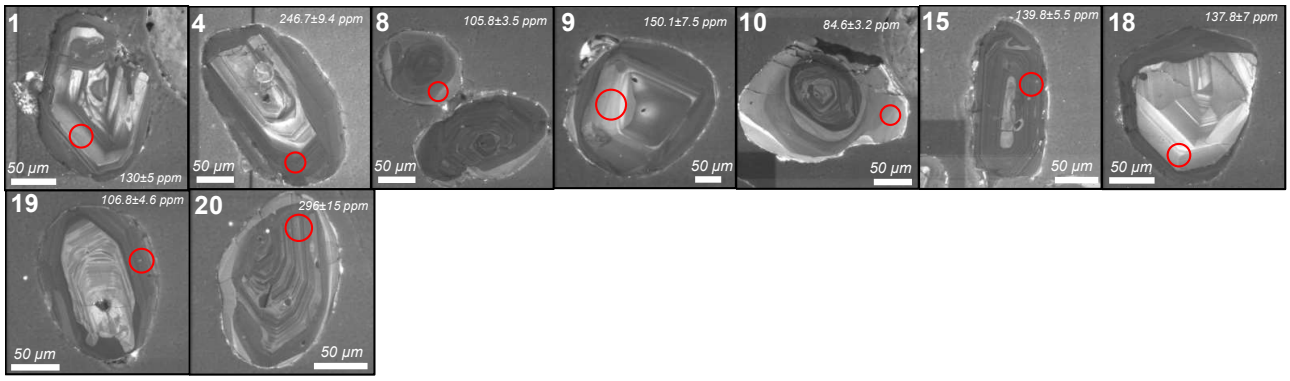

18IM19c

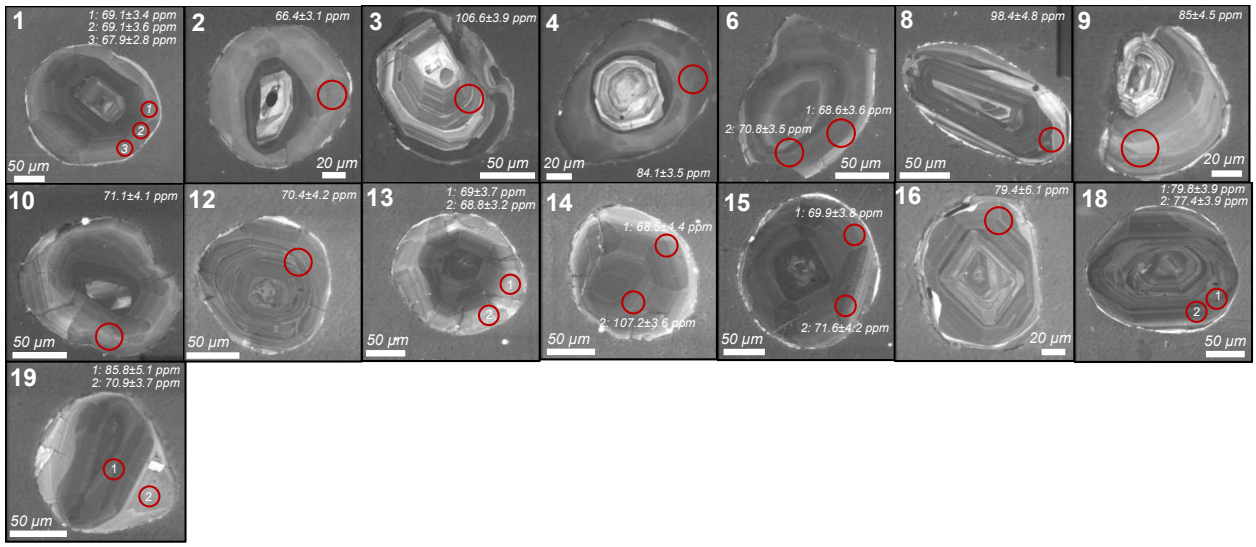

18IM20

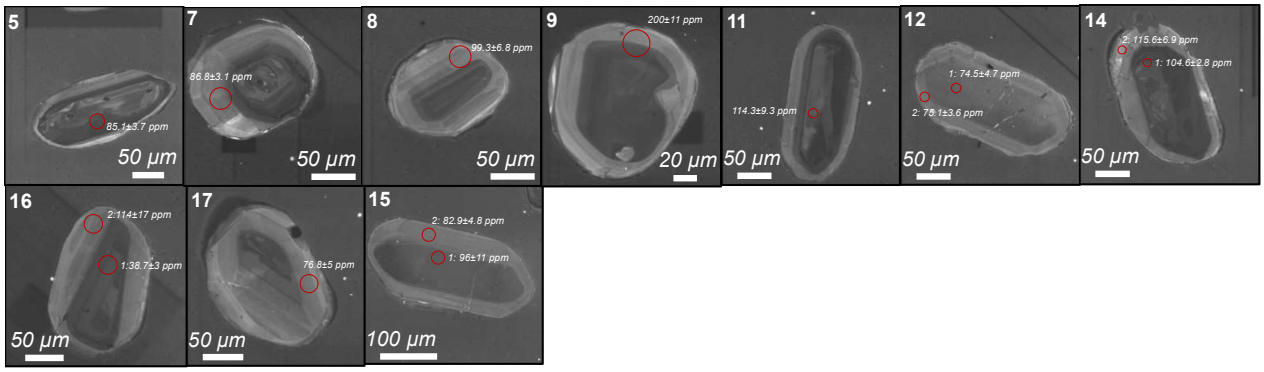

18IM23D

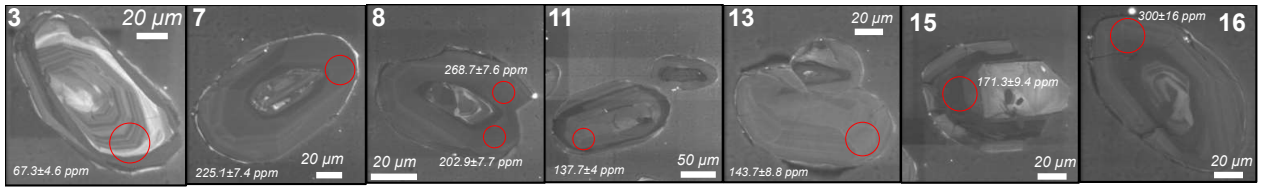

no CL images for 18, 19, 20, 21, 22

18IM21c

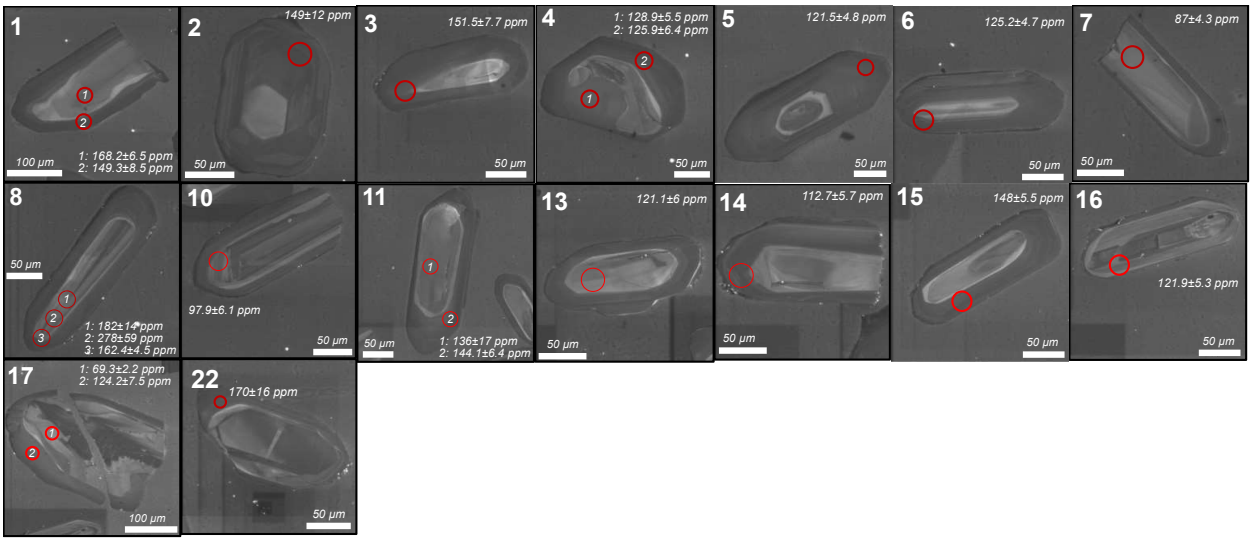

CO-17-8

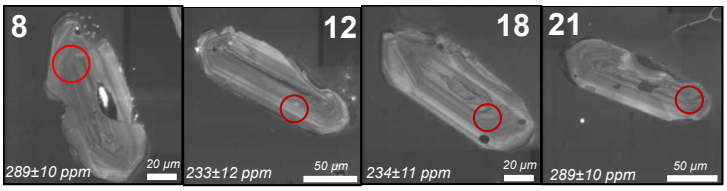

19GH-9

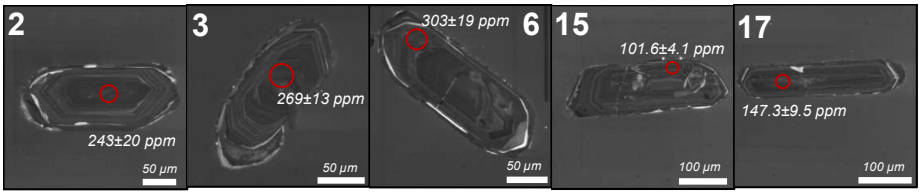

19GH-11B

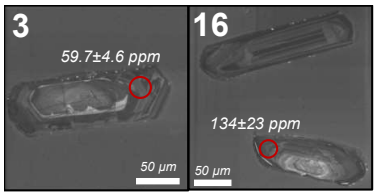

Figure S-2 Measured Y and REE concentrations in reference zircons normalised to reference values. Reference values are from GeoREM (Jochum *et al.,* 2005) for 91500 **(a)** and Piazolo *et al.* (2017) for GJ-1 **(b)**.

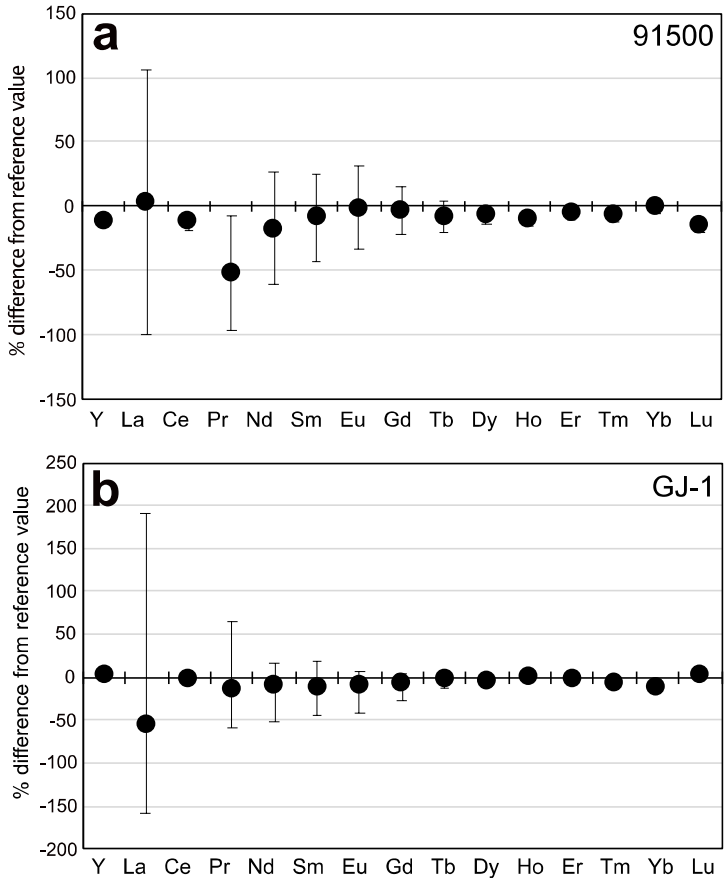

Figure S-3 Comparison of measured intra-zircon phosphorus concentrations for zircon where more than one spot was analysed. Numbers in symbols indicates the analysed grain number. Dashed diagonal lines indicate constant ppm offset (± 25, 50, and 100 ppm) for reference.

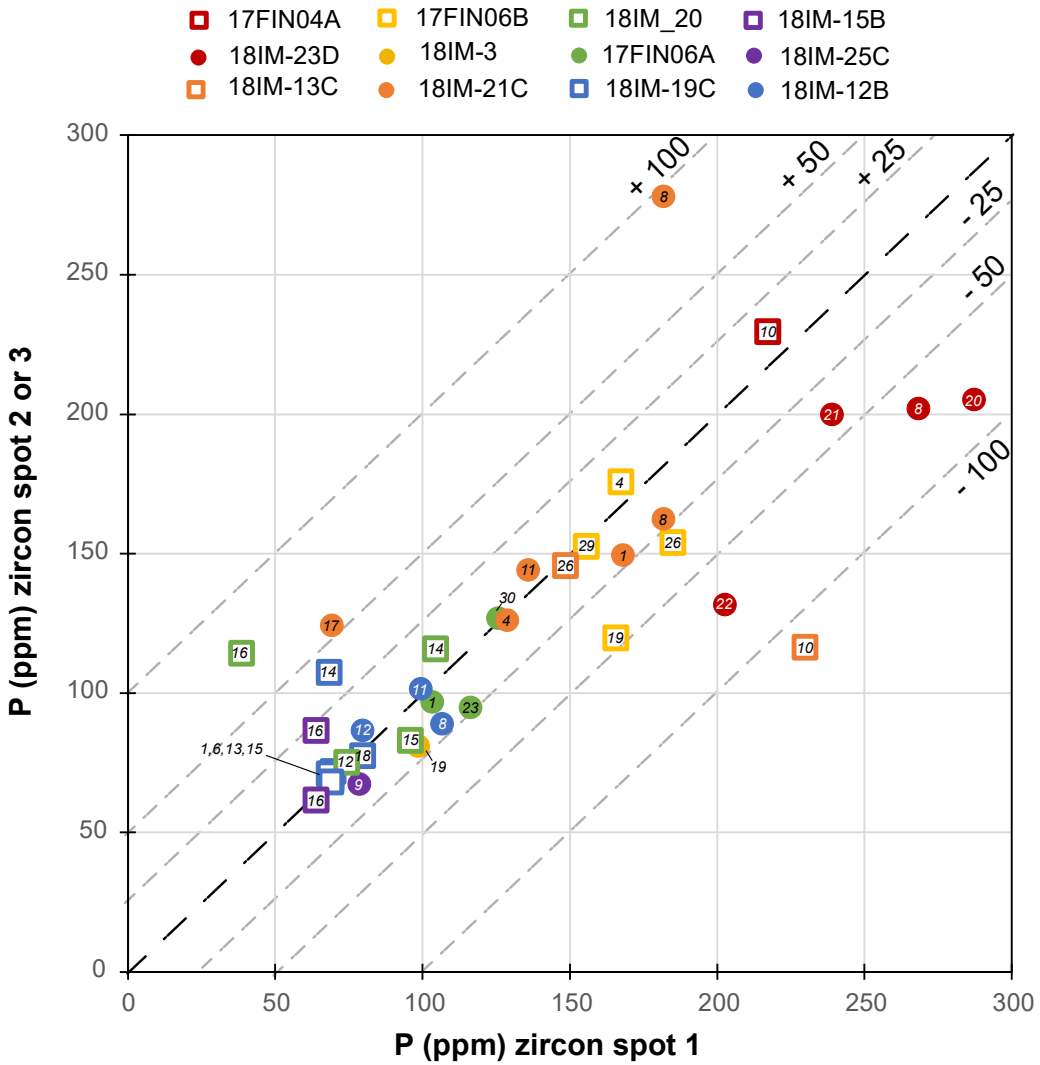

Figure S-4 (a) alphaMELTS modelling results showing variations in melt ASI (molar Al/(Ca+Na+K) and M [molar (Na+K+2Ca)/(Al*Si)] with temperature. ASI and M are strongly correlated due to the similarities in the molar components involved in their calculation. At low temperatures M continues to decrease due to an increase in molar Si, which is not reflected in the ASI. **(b)** Calculated zircon saturation temperatures versus M for both (Harrison and Watson, 1983; Boehnke *et al.*, 2013) for zircon saturation at 150 ppm Zr in the melt (figure modified after Boehnke *et al*., 2013). Blue shaded region indicates range of M values in alphaMELTS modelling (0.9-1.27)

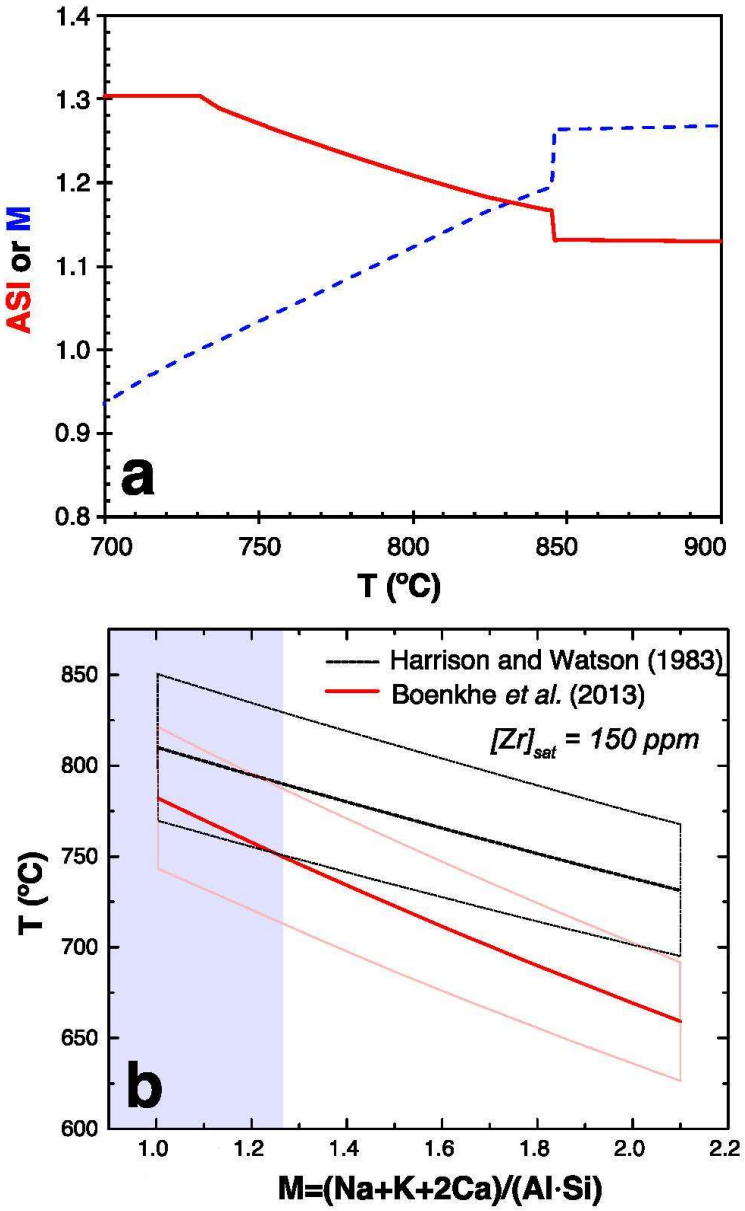

Supplementary Information References

Bea, F., Pereira, M.D., Corretgé, L.G., Fershtater, G.B. (1994) Differentiation of strongly peraluminous, perphosphorus granites: The pedrobernardo pluton, central Spain. *Geochimica et Cosmochimica Acta* 58, 2609–2627 https://doi.org/10.1016/0016-7037(94)90132-5

Black, L.P. *et al.* (2004) Improved $^{206}Pb/^{238}U$ microprobe geochronology by the monitoring of a trace-element-related matrix effect; SHRIMP, ID–TIMS, ELA–ICP–MS and oxygen isotope documentation for a series of zircon standards. *Chemical Geology* 205, 115–140 https://doi.org/10.1016/j.chemgeo.2004.01.003

Boehnke, P., Watson, E.B., Trail, D., Harrison, T.M., Schmitt, A.K. (2013) Zircon saturation re-revisited. *Chemical Geology* 351, 324–334 https://doi.org/10.1016/j.chemgeo.2013.05.028

Bucholz, C.E., Spencer, C.J. (2019) Strongly Peraluminous Granites across the Archean–Proterozoic Transition. *Journal of Petrology* 60, 1299–1348 https://doi.org/10.1093/petrology/egz033

Bucholz, C.E., Stolper, E.M., Eiler, J.M., Breaks, F.W. (2018) A Comparison of Oxygen Fugacities of Strongly Peraluminous Granites across the Archean–Proterozoic Boundary. *Journal of Petrology* 59, 2123–2156 https://doi.org/10.1093/petrology/egy091

Ferry, J.M., Watson, E.B. (2007) New thermodynamic models and revised calibrations for the Ti-in-zircon and Zr-in-rutile thermometers. *Contributions to Mineralogy and Petrology* 154, 429–437 https://doi.org/10.1007/s00410-007-0201-0

Garber, J.M., Smye, A.J., Feineman, M.D., Kylander-Clark, A.R.C., Matthews, S. (2020) Decoupling of zircon U–Pb and trace-element systematics driven by U diffusion in eclogite-facies zircon (Monviso meta-ophiolite, W. Alps). *Contributions to Mineralogy and Petrology* 175, 55 https://doi.org/10.1007/s00410-020-01692-2

Harrison, M.T., Watson, B.E. (1983) Kinetics of Zircon Dissolution and Zirconium Diffusion in Granitic Melts of Variable Water Content. *Contributions to Mineralogy and Petrology* 84, 66–72 https://doi.org/10.1007/BF01132331

Jackson, S.E., Pearson, N.J., Griffin, W.L., Belousova, E.A. (2004) The application of laser ablation-inductively coupled plasma-mass spectrometry to in situ U–Pb zircon geochronology. *Chemical Geology* 211, 47–69 https://doi.org/10.1016/j.chemgeo.2004.06.017

Jochum, K.P., Nohl, U., Herwig, K., Lammel, E., Stoll, B., Hofmann, A.W. (2005) GeoReM: A New Geochemical Database for Reference Materials and Isotopic Standards. *Geostandards and Geoanalytical Research* 29, 333–338 https://doi.org/10.1111/j.1751-908X.2005.tb00904.x

Kylander-Clark, A.R.C., Hacker, B.R., Cottle, J.M. (2013) Laser-ablation split-stream ICP petrochronology. *Chemical Geology* 345, 99–112 https://doi.org/10.1016/j.chemgeo.2013.02.019

Liebmann, J., Spencer, C.J., Kirkland, C.L., Bucholz, C., He, X., Santosh, M., Xia, X.P., Martin, L., Evans, N.J. (2021a) Emergence of continents above sea‐level influences sediment melt composition. *Terra Nova* 33, 465–474 https://doi.org/10.1111/ter.12531

Liebmann, J., Spencer, C.J., Kirkland, C.L., Bucholz, C.E., Xia, X.-P., Martin, L., Kitchen, N., Shumlyanskyy, L. (2021b) Coupling sulfur and oxygen isotope ratios in sediment melts across the Archean-Proterozoic transition. *Geochimica et Cosmochimica Acta* 307, 242–257 https://doi.org/10.1016/j.gca.2021.05.045

Liebmann, J., Spencer, C.J., Kirkland, C.L., Xia, X.-P., Bourdet, J. (2021c) Effect of water on $\delta^{18}O$ in zircon. *Chemical Geology* 574, 120243 https://doi.org/10.1016/j.chemgeo.2021.120243

London, D. (1992) Phosphorus in S-type magmas: The P_2O_5 content of feldspars from peraluminous magmas, pegmatite, and rhyolites. *American Mineralogist* 77, 126–145

Paces, J.B., Miller, J.D.J. (1993) Precise U–Pb ages of Duluth Complex and related mafic intrusions, northeastern Minnesota: geochronological insights to physical, petrogenetic, paleomagnetic, and tectonomagmatic processes associated with the 1.1 Ga Midcontinent Rift System. *Journal of Geophysical Research* 98, 13997-14013 https://doi.org/10.1029/93JB01159

Paton, C., Hellstrom, J., Paul, B., Woodhead, J., Hergt, J. (2011) Iolite: Freeware for the visualisation and processing of mass spectrometric data. *Journal of Analytical Atomic Spectrometry* 26, 2508 https://doi.org/10.1039/c1ja10172b

Piazolo, S., Belousova, E., La Fontaine, A., Corcoran, C., Cairney, J.M. (2017) Trace element homogeneity from micron- to atomic scale: Implication for the suitability of the zircon GJ-1 as a trace element reference material. *Chemical Geology* 456, 10–18 https://doi.org/10.1016/j.chemgeo.2017.03.001

Pichavant, M., Montel, J.-M., Richard, L.R. (1992) Apatite solubility in peraluminous liquids: Experimental data and an extension of the Harrison-Watson model. *Geochimica et Cosmochimica Acta* 56, 3855–3861 https://doi.org/10.1016/0016-7037(92)90178-L

Schiller, D., Finger, F. (2019) Application of Ti-in-zircon thermometry to granite studies: problems and possible solutions. *Contributions to Mineralogy and Petrology* 174, 51 https://doi.org/10.1007/s00410-019-1585-3

Sláma, J. *et al.* (2008) Plešovice zircon — A new natural reference material for U–Pb and Hf isotopic microanalysis. *Chemical Geology* 249, 1–35 https://doi.org/10.1016/j.chemgeo.2007.11.005

Smith, P.M., Asimow, P.D. (2005) Adiabat_1ph: A new public front-end to the MELTS, pMELTS, and pHMELTS models: ADIABAT_1PH FRONT-END. *Geochemistry, Geophysics, Geosystems* 6 https://doi.org/10.1029/2004GC000816

Stepanov, A.S., Hermann, J., Rubatto, D., Rapp, R.P. (2012) Experimental study of monazite/melt partitioning with implications for the REE, Th and U geochemistry of crustal rocks. *Chemical Geology* 300–301, 200–220 https://doi.org/10.1016/j.chemgeo.2012.01.007

Stern, R.A., Bodorkos, S., Kamo, S.L., Hickman, A.H., Corfu, F. (2009) Measurement of SIMS Instrumental Mass Fractionation of Pb Isotopes During Zircon Dating. *Geostandards and Geoanalytical Research* 33, 145–168 https://doi.org/10.1111/j.1751-908X.2009.00023.x

Wiedenbeck, M. *et al.* (2004) Further Characterisation of the 91500 Zircon Crystal. *Geostandards and Geoanalytical Research* 28, 9–39 https://doi.org/10.1111/j.1751-908X.2004.tb01041.x

Wiedenbeck, M., Allé, P., Corfu, F., Griffin, W.L., Meier, M., Oberli, F., Quadt, A.V., Roddick, J.C., Spiegel, W. (1995) Three Natural Zircon Standards for U-Th-Pb, Lu-Hf, Trace Element and REE Analyses. *Geostandards and Geoanalytical Research* 19, 1–23. https://doi.org/10.1111/j.1751-908X.1995.tb00147.x

Wolf, M.B., London, D. (1995) Incongruent dissolution of REE- and Sr-rich apatite in peraluminous granitic liquids; differential apatite, monazite, and xenotime solubilities during anatexis. *American Mineralogist* 80, 765–775. https://doi.org/10.2138/am-1995-7-814